

Research Article

Bistatic ISAR Sparse Imaging Method for High-Speed Moving Target Based on Dechirping Processing

Chuangzhan Zeng , Weigang Zhu, and Xin Jia

Space Engineering University, Beijing 101416, China

Correspondence should be addressed to Chuangzhan Zeng; zocle@bupt.edu.cn

Received 22 June 2018; Revised 21 September 2018; Accepted 30 September 2018; Published 27 January 2019

Academic Editor: Angelo Liseno

Copyright © 2019 Chuangzhan Zeng et al. This is an open access article distributed under the Creative Commons Attribution License, which permits unrestricted use, distribution, and reproduction in any medium, provided the original work is properly cited.

Bistatic inverse synthetic aperture radar (ISAR) can increase the probability of tracking the high-speed target and provide more angle information than monostatic ISAR. However, bistatic ISAR suffers from a serious defocusing problem, resulting from the high-speed motion. Furthermore, the inherent geometry distortion and calibration problems make bistatic ISAR (B-ISAR) imaging more complex. In response to these problems, we propose a bistatic ISAR imaging method for high-speed moving target with geometric distortion correction and calibration based on dechirping processing. At first, based on the motion decomposition idea, the B-ISAR echo model of the high-speed moving target is established. Then, by analyzing the imaging mechanism of the Range-Doppler algorithm (RDA), we eliminate the phase items influencing the imaging quality with speed compensation and Doppler compensation. After that, the analytic formula of the geometric distortion factor and calibration factor are deduced, which helps transform the geometric correction and calibration problem into a parameter estimation problem. Finally, with the sparsity of the scattering points, the required parameters are solved using the expectation maximization (EM) algorithm based on the maximum a posteriori probability criterion. With the estimated parameters, a clear B-ISAR image of a high-speed moving target with geometric correction and calibration is obtained. The simulations show that the proposed method has a better resolution and simultaneously attains geometric correction and calibration of the image.

1. Introduction

Inverse synthetic aperture radar (ISAR) can obtain two-dimensional (2D) images of a target, which plays an important role in some fields, such as target tracking and recognition [1, 2]. However, the monostatic ISARs suffer from some problems, such as imaging a target moving along the line of sight, detecting the stealthy target, and tracking the high-speed target.

To overcome these limitations, a bistatic ISAR (B-ISAR) imaging method is proposed with a separate transmitter and receiver [3–6]. B-ISAR can provide more observation angles than monostatic ISAR, so that the desired cross-range angle is ensured to image the target moving along the line of sight. Otherwise, multiple look angle and higher transmission gain help B-ISAR to detect the stealthy target. In addition, the separate arrangement of the transmitter and receiver not only increases the probability of tracking the high-speed

target but also is more immune to jamming, more secure, and more flexible.

Although B-ISAR has many advantages, the complexity of its imaging geometry leads to its difficulty in application. To simplify the expression of the echo, most of the current studies [4–10] adopted the idea of equivalence, so the B-ISAR is regarded as a monostatic radar in the bistatic angular bisector direction. Then, the traditional monostatic ISAR imaging algorithm is used [4, 5]. However, the bistatic angle changes along with the movement of the target. For this situation, the RDA resulted in a blurred and defocused image. For this, Martorella et al. [3, 6] performed the Taylor expansion on the bistatic angle. The point spread function (PSF) of bistatic ISAR was obtained, and the distortion caused by bistatic ISAR imaging geometry was analyzed. The time-varying bistatic angle was further extended to three-dimensional (3D) space, and spatial-variant property of imaging plane was discussed [7]. Based on the Taylor

expansion, the Doppler migration caused by geometric distortion of B-ISAR and the migration caused by the target motion was combined [8]. They derived the phase shift function and compensated for the shifted phase by estimating the shift factor. Then the image was corrected according to the geometric characteristics of the target image. Unfortunately, the geometric characteristics of the target image are usually difficult to obtain, so the geometric distortion factor is hard to estimate. Additionally, the complexity of the B-ISAR imaging geometry complicates the accurate calibration of the image.

To achieve geometric distortion correction and calibration of B-ISAR, Kang et al. [9, 10] introduced the concept of equivalent rotation velocity (ERV) and derived the analytical relationship between the geometric distortion factor, calibration factor, system parameters, and target motion parameters by Taylor expansion. With this concept, the geometric correction and calibration problem was transformed into a parameter estimation problem. Cataldo and Martorella [11] derived the analytic constraints for B-ISAR distortion due to range and Doppler migration, and then proposed a reduction method of B-ISAR distortion based on the super-resolution techniques such as bandwidth extrapolation (BWE), Super-SVA (SSVA), and compressed sensing (CS).

The above methods were all based on the idea of equivalent and Taylor expansion, which ignored the B-ISAR's unique triangular geometric relation, forming a deep coupling between the range and cross range that cannot fully reflect the main characteristic of B-ISAR. Different from these methods, Chai et al. [12] proposed a bistatic ISAR imaging method based on the motion decomposition model. The geometric distortion factor and calibration factor were described by the bistatic angle and the rotation rate of the target relative to the transmitter and receiver, and then the parameters were estimated with the sparse decomposition method, to create sparse imaging algorithm with geometric distortion correction and calibration.

However, with the emergence of all kinds of high-speed aircrafts and the increasing demand for imaging of unknown space targets, the research into B-ISAR imaging methods for high-speed moving targets has attracted attention. Since the echoes of the high-speed target do not satisfy the traditional "stop-go" model, the Taylor expansion method and motion decomposition method are both no longer valid. According to Zhang et al. [13], the idea of speed compensation function from monostatic ISAR was used to deal with the effect of high-speed motion, and the quadratic phase caused by high-speed motion was eliminated using fractional Fourier transform (FrFT), but the imaging accuracy was limited by the length of the FrFT search step. Xiao et al. [14] established the echo model of the high-speed target and treated it as the linear frequency-modulated signals. With the discrete chirp-Fourier transform (DCFT) method, the speed can be estimated and the influence of the high-speed moving can be compensated. However, when the motion is not uniform, the method is no longer valid. Han et al. [15] deduced the expression of the compensation term relative to the frequency in fast time domain and the speed. Then, the sparsity of echoes was used to construct a redundant dictionary to

estimate the speed. Guo and Shang [16] constructed the speed compensation function by approximating the speed and distance of all scattering points to the ones of the target center, but the center speed is hard to obtain as well. The methods mentioned above all address the idea of speed compensation, which only aims at solving the problems caused by high-speed motion. For the inherent B-ISAR geometric distortion and calibration problem, further research is still required.

As we described, for a clear B-ISAR image of high-speed moving targets, there are three problems to solve: (a) the influence of the high-speed motion, (b) geometry distortion by B-ISAR, and (c) range and cross range calibration. To the best of our knowledge to date, however, there has yet been no research conducted on these problems simultaneously.

In this paper, we proposed an improved method based on the motion decomposition method [12]. At first, by analyzing the B-ISAR imaging geometry of high-speed targets and eliminating the phase items influencing the image quality using speed and Doppler compensation, the analytical expressions of the geometry distortion factor and calibration factor are derived. Then, using the sparse decomposition idea, the distortion correction and calibration problem is transformed into a sparse signal parametric optimization problem. Finally, the distortion correction and calibration of the image are simultaneously realized with the sparse imaging using the expectation maximization (EM) algorithm.

2. B-ISAR Echo Modelling of High-Speed Target Based on Motion Decomposition

2.1. Imaging Geometry of B-ISAR. The B-ISAR imaging geometry is shown in Figure 1. The reference point O on the target is regarded as the origin of the coordinate, the direction of the bistatic angle bisector at $t_m = 0$ as the y -axis, and the plane constructed by the transmitter, receiver, and target at $t_m = 0$ as coordinate xOy , assuming that the coordinate system moves with the target during the imaging period.

The distance vectors from the transmitter and receiver to the reference point are \mathbf{R}_t and \mathbf{R}_r , respectively. During the imaging period, the target moves linearly at speed $\mathbf{v} = (v, \theta)$, where v is a constant and θ is the angle between \mathbf{v} and the x -axis.

Assuming that the effective rotation vectors of the target relative to the transmitter and receiver are ω_t and ω_r , respectively [12]. Let $\beta_t(t_m) = \beta_0 + \omega_t t_m$ be the angle between $\mathbf{R}_t(t_m)$ and y axis, and $\beta_r(t_m) = \beta_0 - \omega_r t_m$ be the angle between $\mathbf{R}_r(t_m)$ and y axis, where β_0 is the half bistatic angle at $t_m = 0$, and $\omega_t = |\omega_t|$, $\omega_r = |\omega_r|$.

Known from the far field approximation condition is $r(\mathbf{s}, t_m) = |\mathbf{R}(t_m) + \mathbf{s}| \approx |\mathbf{R}(t_m)| + \mathbf{s} \cdot \hat{\mathbf{R}}(t_m)$. The unit vectors of \mathbf{R}_t and \mathbf{R}_r are $\hat{\mathbf{R}}_t = (\sin \beta_t, \cos \beta_t)$ and $\hat{\mathbf{R}}_r = (\sin \beta_r, \cos \beta_r)$, respectively. Substituting $\beta_t(t_m)$ and $\beta_r(t_m)$ into the unit vectors, we obtain the slant distance between the scattering point on the target $\mathbf{s} = (x, y)$ and the transmitter as $r_t(\mathbf{s}, t_m) \approx |\mathbf{R}_t(t_m)| + x \sin \beta_t(t_m) + y \cos \beta_t(t_m)$. Similarly, the distance from the scattering point \mathbf{s} to the receiver is $r_r(\mathbf{s}, t_m) \approx |\mathbf{R}_r(t_m)| - x \sin \beta_r(t_m) + y \cos \beta_r(t_m)$.

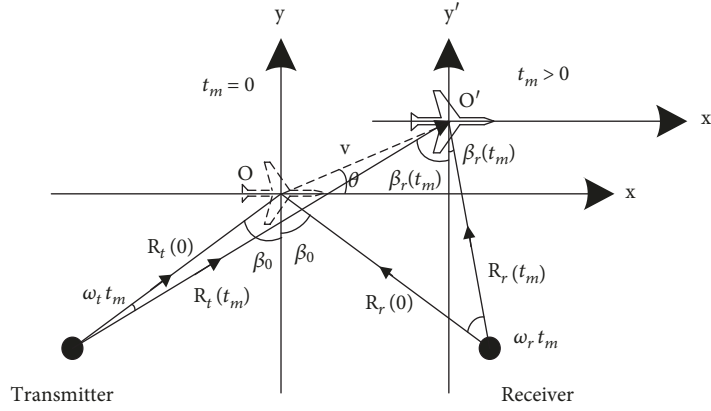


FIGURE 1: Bistatic inverse synthetic aperture radar (B-ISAR) imaging geometry.

2.2. *B-ISAR Echo Model of High-Speed Target.* Assuming that the radar signal transmitted is a wideband linear frequency modulation (LFM) signal, the waveform is

$$s_t(\hat{t}) = A s_\omega(\hat{t}) \exp(j2\pi f_c t), \quad (1)$$

where A is the signal amplitude, f_c is the carrier frequency, \hat{t} is the fast time, $t = \hat{t} + mT_r$ is the total time, T_r is the pulse repetition interval, $\gamma = B/T_p$ is the modulation rate, and T_p is the pulse width. Considering the transmission delay τ_m , the m th pulse echo can be expressed as

$$s_m(\hat{t}) = A_0 s_\omega(\hat{t} - \tau_m) \exp[j2\pi f_c(\hat{t} - \tau_m)], \quad (2)$$

where $m = 0, 1, \dots, M-1$, M is the number of pulses, and A_0 is the amplitude of the echo.

Assuming τ_{ref} is the reference delay, the dechirping processing reference signal is

$$s_c(\hat{t}) = s_\omega(\hat{t} - \tau_{\text{ref}}) \exp[j2\pi f_c(\hat{t} - \tau_{\text{ref}})]. \quad (3)$$

Multiplying equation (2) to the conjugate of equation (3) results in [17]

$$s_c(\hat{t}) = s_m(\hat{t}) \cdot s_{\text{ref}}^*(\hat{t}) = A_0 \text{rect}\left(\frac{\hat{t} - \tau_m}{T_p}\right) \exp(j\pi\gamma\tau_\Delta^2) \cdot \exp(-j2\pi f_c\tau_\Delta) \exp[-j2\pi\gamma\tau_\Delta(\hat{t} - \tau_{\text{ref}})], \quad (4)$$

where $\tau_\Delta = \tau_m - \tau_{\text{ref}}$ is the difference delay.

We defined v_{Tm} and v_{Rm} as the radial velocity of the target relative to the transmitter and receiver, respectively, assuming that the direction away from the radar is positive, at t_m . The time required to transmit the signal is $t_m + \tilde{t}$, the delay of the transmit signal at the scattering point is τ_1 , and the required time from the scattering point to the receiver is τ_2 . Then [16]

$$c\tau_1 = R_T(t_m + \tilde{t} + \tau_1) \approx r_t(\mathbf{s}, t_m) + v_{Tm}\tilde{t} + v_{Tm}\tau_1, \quad (5)$$

$$c\tau_2 = R_R(t_m + \tilde{t} + \tau_1) \approx r_r(\mathbf{s}, t_m) + v_{Rm}\tilde{t} + v_{Rm}\tau_1. \quad (6)$$

Combining equations (5) and (6), the bistatic echo delay τ_m is

$$\tau_m = \tau_1 + \tau_2 = \frac{v_{Tm} + v_{Rm}}{c - v_{Tm}} \tilde{t} + \frac{r_t(\mathbf{s}, t_m) + r_r(\mathbf{s}, t_m)}{c} + \frac{(v_{Tm} + v_{Rm}) \cdot r_t(\mathbf{s}, t_m)}{c(c - v_{Tm})}. \quad (7)$$

Then the total duration of the echo received by the receiver is

$$t = t_m + \tilde{t} + \tau_m = t_m + \frac{c + v_{Rm}}{c - v_{Tm}} \tilde{t} + \frac{r_t(\mathbf{s}, t_m) + r_r(\mathbf{s}, t_m)}{c} + \frac{(v_{Tm} + v_{Rm}) \cdot r_t(\mathbf{s}, t_m)}{c(c - v_{Tm})}. \quad (8)$$

From equation (8), the relationship between the transmission time \tilde{t} and the reception time \hat{t} is

$$\begin{aligned} \tilde{t} &= \frac{c - v_{Tm}}{c + v_{Rm}} (t - t_m) - \frac{(c - v_{Tm})[r_t(\mathbf{s}, t_m) + r_r(\mathbf{s}, t_m)]}{c(c + v_{Rm})} \\ &\quad - \frac{(v_{Tm} + v_{Rm}) \cdot r_t(\mathbf{s}, t_m)}{c(c + v_{Rm})} \\ &= \frac{c - v_{Tm}}{c + v_{Rm}} \hat{t} - \frac{(c - v_{Tm})[r_t(\mathbf{s}, t_m) + r_r(\mathbf{s}, t_m)]}{c(c + v_{Rm})} \\ &\quad - \frac{(v_{Tm} + v_{Rm}) \cdot r_t(\mathbf{s}, t_m)}{c(c + v_{Rm})}. \end{aligned} \quad (9)$$

Substituting equation (9) into equation (7),

$$\tau_m = \frac{v_{Tm} + v_{Rm}}{c + v_{Rm}} \hat{t} + \frac{r_t(\mathbf{s}, t_m) + r_r(\mathbf{s}, t_m)}{c} - \frac{(v_{Tm} + v_{Rm}) \cdot r_r(\mathbf{s}, t_m)}{c(c + v_{Rm})}. \quad (10)$$

Substituting equation (10) into equation (4) and rearranging the formula provides

$$\begin{aligned}
s_c(\bar{t}) &= A_0 \text{rect} \left(\frac{\bar{t} - \tau_{im} - p_v \bar{t}}{T_p} \right) \exp \left[j\pi\gamma(p_v \bar{t} + \tau_{im} - \tau_{ref})^2 \right] \\
&\cdot \exp \left[-j2\pi f_c(p_v \bar{t} + \tau_{im} - \tau_{ref}) \right] \\
&\times \exp \left[-j2\pi\gamma(\bar{t} - \tau_{ref})(p_v \bar{t} + \tau_{im} - \tau_{ref}) \right] \\
&= A_0 \text{rect} \left[\frac{(\bar{t} - \tau_{ref})(1 - p_v) - (\tau_{im} - \tau_{ref} + p_v \tau_{ref})}{T_p} \right] \\
&\cdot \exp \left\{ j\pi(\gamma p_v^2 - 2\gamma p_v)\bar{t}^2 \right\} \\
&\times \exp \left\{ j\pi[2\gamma\tau_{im}p_v - 2f_c p_v - 2\gamma\tau_{im} + 2\gamma\tau_{ref}]\bar{t} \right\} \\
&\cdot \exp \left\{ j\pi[\gamma\tau_{im}^2 - \gamma\tau_{ref}^2 - 2f_c\tau_{im} + 2f_c\tau_{ref}] \right\}, \tag{11}
\end{aligned}$$

where $\tau_{im} = \tau_m - p_v \hat{t}$ is a function of t_m , $p_v = (v_{Tm} + v_{Rm}) / (c + v_{Rm})$. Considering $v_{Tm} \ll c$ and $v_{Rm} \ll c$, and assigning $\bar{t} = \hat{t} - \tau_{ref}$, which uses the reference point as the starting point of the fast time, then [18]

$$\begin{aligned}
s_c(\bar{t}) &= A_0 \text{rect} \left[\frac{\bar{t} - (\tau_{im} - \tau_{ref} + p_v \tau_{ref})}{T_p} \right] \\
&\cdot \exp \left[-j2\pi(\phi_1 + \phi_2 + \phi_3 \bar{t} + \phi_4 \bar{t}^2) \right], \tag{12} \\
\phi_1 &= f_c(p_v \tau_{ref} + \tau_{im} - \tau_{ref}), \\
\phi_2 &= -\frac{\gamma}{2}(p_v \tau_{ref} + \tau_{im} - \tau_{ref})^2, \\
\phi_3 &= [\gamma(p_v \tau_{ref} + \tau_{im} - \tau_{ref})(1 - p_v) + f_c p_v], \\
\phi_4 &= \left[\gamma p_v \left(1 - \frac{p_v}{2} \right) \right].
\end{aligned}$$

From equation (12), after dechirping processing, four phase items exist in the expression of the echo. Among them, $\phi_4 \bar{t}^2$ is a quadratic function of the fast time \bar{t} , which broadens the range profile so compensation is required (for more details please refer to [19]). $\phi_3 \bar{t}$ is a linear function about \bar{t} that appears as the ‘‘walk’’ of the range profile peak in the frequency domain, which can be eliminated by translational compensation. $(\phi_1 + \phi_2)$ is a constant term of \bar{t} that has no effect on the range profile but contributes to the subsequent Doppler analysis of 2D imaging, in which ϕ_1 is a linear phase term and ϕ_2 is a residual video phase (RVP) term.

3. B-ISAR Range-Doppler Imaging Analysis of High-Speed Targets

3.1. Speed Compensation. From equation (12), each echo is a linear frequency modulation (LFM) signal in the fast time domain after dechirping processing. So, modified discrete chirp transform (DCT) [20] can be used to estimate the chirp rate, and then the phase compensation function is constructed to eliminate the quadratic phase term with the estimated parameters. Assuming that the estimated chirp rate is $\bar{\gamma}_m$, the phase compensation function can be constructed as

$$s_{cmp}(\bar{t}) = \exp \left(j\pi \bar{\gamma}_m \bar{t}^2 \right). \tag{13}$$

Then, after compensation, we obtain

$$\begin{aligned}
s(\bar{t}) &= s_c(\bar{t}) \cdot s_{cmp}^*(\bar{t}) \\
&= A_0 \text{rect} \left[\frac{\bar{t} - (\tau_{im} - \tau_{ref} + p_v \tau_{ref})}{T_p} \right] \\
&\times \exp \left\{ -j2\pi(\phi_1 + \phi_2 + \phi_3 \bar{t}) \right\}. \tag{14}
\end{aligned}$$

Apply FFT to \bar{t} in equation (14), then

$$\begin{aligned}
S(f_i) &= A_1 \sin c \left[T_p(f_i + \phi_3) \right] \exp \left\{ -j2\pi(\phi_1 + \phi_2) \right\} \\
&\cdot \exp \left[-j2\pi f_i(\tau_{im} - \tau_{ref}) \right] \exp \left(-j2\pi f_i p_v \tau_{ref} \right), \tag{15}
\end{aligned}$$

where ϕ_3 is the amount of range walk generated by the first-order phase term, and

$$\begin{aligned}
\phi_3 &= [\gamma(1 - p_v)(\tau_{im} - \tau_{ref}) + \gamma p_v \tau_{ref}(1 - p_v) + f_c p_v] \\
&= \phi_0 + \phi'_0 t_m + o(t_m), \tag{16}
\end{aligned}$$

where ϕ_0 is a constant term, and the variation term $\phi'_0 t_m + o(t_m)$ can be corrected by the translational compensation method of the monostatic ISAR. After correction, the echo at the range unit $f_i = -\phi_0$ is

$$\begin{aligned}
S(f_i, t_m) &= A_1 \sin c \left[T_p(f_i + \phi_0) \right] \exp \left\{ -j2\pi(\phi_1 + \phi_2) \right\} \\
&\cdot \exp \left[-j2\pi f_i(\tau_{im} - \tau_{ref}) \right] \exp \left(-j2\pi f_i p_v \tau_{ref} \right) \\
&= A_2 \text{sinc} \left[T_p(f_i + \phi_0) \right] \times \exp \left\{ j\pi\gamma\tau_{im}^2 \right\} \\
&\cdot \exp \left\{ -j2\pi[f_c + \gamma(1 - p_v)\tau_{ref} + f_i]\tau_{im} \right\} \\
&\times \exp \left\{ j2\pi \left[(f_c + f_i)\tau_{ref}(1 - p_v) \right. \right. \\
&\quad \left. \left. + \frac{\gamma}{2}(1 - p_v)^2 \tau_{ref}^2 \right] \right\}. \tag{17}
\end{aligned}$$

3.2. Doppler Compensation. Known from equation (17), the echo is a quadratic phase function with respect to τ_{im} , and τ_{im} defined in equation (11) is

$$\begin{aligned}
\tau_{im} &= \frac{r_t(\mathbf{s}, t_m) + r_r(\mathbf{s}, t_m)}{c} - \frac{(v_{Tm} + v_{Rm}) \cdot r_r(\mathbf{s}, t_m)}{c(c + v_{Rm})} \\
&= \frac{(c + v_{Rm}) \cdot r_t(\mathbf{s}, t_m) + (c - v_{Tm}) \cdot r_r(\mathbf{s}, t_m)}{c(c + v_{Rm})}. \tag{18}
\end{aligned}$$

Substitute $r_t(\mathbf{s}, t_m)$ and $r_r(\mathbf{s}, t_m)$ defined in Section 2.1, then

$$\begin{aligned}
\tau_{im} &= \frac{(c + v_{Rm}) \cdot [|\mathbf{R}_t(t_m)| + x \sin \beta_t(t_m) + y \cos \beta_t(t_m)]}{c(c + v_{Rm})} \\
&+ \frac{(c - v_{Tm}) \cdot [|\mathbf{R}_r(t_m)| - x \sin \beta_r(t_m) + y \cos \beta_r(t_m)]}{c(c + v_{Rm})}. \tag{19}
\end{aligned}$$

If the target motion is stable and the relative rotation angle is small enough in conjunction with the B-ISAR imaging geometry shown in Figure 1, the above formula can be simplified as (Appendix A)

$$\tau_{im} \approx K_0 + K_1 t_m, \quad (20)$$

where

$$K_0 \approx \frac{|\mathbf{R}_t(0)| + |\mathbf{R}_r(0)|}{c} + \frac{2y \cos \beta_0 - 2v_0/c \cdot |\mathbf{R}_r(0)| \cdot \sin \theta \cos \beta_0}{c + v_0 \sin(\theta - \beta_0)}, \quad (21)$$

$$K_1 \approx \frac{(x - (v_0 \cos \theta \cdot |\mathbf{R}_r(0)|/c))(\omega_t + \omega_r) \cos \beta_0 + (y - (v_0 \sin \theta \cdot |\mathbf{R}_r(0)|/c))(\omega_r - \omega_t) \sin \beta_0 + 2v_0 \sin \theta \cos \beta_0}{c + v_0 \sin(\theta - \beta_0)}. \quad (22)$$

When v_0 is small enough (satisfies $v_0 \cdot |\mathbf{R}_r(0)|/c^2 \ll 1$) and $\theta = 0$, equation (20) can be simplified as

$$\tau_{im} = \frac{|\mathbf{R}_t(t_m)| + |\mathbf{R}_r(t_m)|}{c} + \frac{2y \cos \beta_0 + x(\omega_t + \omega_r) \cos \beta_0 + y(\omega_r - \omega_t) \sin \beta_0}{c}, \quad (23)$$

which is the same as the formula previously derived in [12].

When $v_0 \cdot |\mathbf{R}_r(0)|/c^2 \ll 1$ is not satisfied, since $K_1 \propto x \propto t_m$, then assuming $K_1 = K_{10} + K_{11} t_m$, substitute equation (20) into equation (17):

$$\begin{aligned} S(f_i, t_m) &= A_2 \text{sinc} [T_p(f_i + \phi_0)] \exp(j\pi\gamma K_{11}^2 t_m^4) \\ &\cdot \exp(j2\pi\gamma K_{10} K_{11} t_m^3) \exp(j\pi\gamma K_{10}^2 t_m^2) \\ &\times \exp\{-j2\pi K_1 [f_c + \gamma(1 - p_v)\tau_{\text{ref}} + f_i - \gamma K_0] t_m\} \\ &\times \exp\{j\pi[\gamma(1 - p_v)^2 \tau_{\text{ref}}^2 \\ &\quad + 2(f_c + f_i - \gamma K_0)\tau_{\text{ref}}(1 - p_v) \\ &\quad + \gamma K_0^2 - 2K_0(f_c + f_i)]\}. \end{aligned} \quad (24)$$

Known from equation (22), $\gamma K_{11}^2 \approx \gamma/c^2 \ll 1$, so the phase term $\exp(j\pi\gamma K_{11}^2 t_m^4)$ can be negligible, and therefore, the echo can be regarded as a cubic phase function with respect to t_m [21]. The cubic phase function (CPF) [22] can be used to estimate the third-order phase coefficient $\bar{\eta}_1$ and the second-order coefficient $\bar{\eta}_2$. With them, the phase compensation function can be constructed as $S_{\text{comp}}(t_m) = \exp[j\pi(\bar{\eta}_1 t_m^3 + \bar{\eta}_2 t_m^2)]$, and after Doppler compensation, the echo is

$$\begin{aligned} S_c(f_i, t_m) &= S(f_i, t_m) \cdot S_{\text{comp}}^*(t_m) \\ &= A_2 \text{sinc} [T_p(f_i + \phi_0)] \exp(j2\pi f_{di} t_m) \exp(j\phi), \end{aligned} \quad (25)$$

where $f_{di} = \gamma K_0 K_1 - f_c K_1 - f_i K_1 - \gamma K_1(1 - p_v)\tau_{\text{ref}}$ is the Doppler frequency, $\phi = \pi[\gamma(1 - p_v)^2 \tau_{\text{ref}}^2 + 2(f_c + f_i - \gamma K_0)\tau_{\text{ref}}(1 - p_v) + \gamma K_0^2 - 2K_0(f_c + f_i)]$.

3.3. *RD Imaging and the Calibration Relationship.* Apply Fourier transform to t_m in equation (25), and then attain the imaging result as

$$s_{dc}(f_i, f_d) = A_3 \text{sinc} [T_p(f_i + \phi_0)] \cdot \text{sinc} [T_m(f_d - f_{di})] \exp(j\phi), \quad (26)$$

where f_d is the rotation Doppler.

Equations (16) and (20) show that

$$\begin{aligned} \phi_3 &= [\gamma(1 - p_v)(\tau_{im} - \tau_{\text{ref}} + p_v \tau_{\text{ref}}) + f_c p_v] = \gamma K_1(1 - p_v)t_m \\ &\quad + [\gamma K_0(1 - p_v) - \gamma(1 - p_v)^2 \tau_{\text{ref}} + f_c p_v] = \phi_0' t_m + \phi_0. \end{aligned} \quad (27)$$

Then, known from the first Sinc function of equation (26) and ϕ_0 in equation (27), the calibration relationship between the ordinate y of the scattering point and the frequency f_i of the fast time is

$$\begin{aligned} f_i &= (1 - p_v)[\gamma(1 - p_v)\tau_{\text{ref}} - \gamma K_0 + f_c] - f_c \\ &\approx \gamma(\tau_{\text{ref}} - K_0). \end{aligned} \quad (28)$$

From the second Sinc function of equation (26), the calibration relationship between the ordinates (x, y) of the scattering point and the rotation Doppler f_d is

$$\begin{aligned} f_d &= \gamma K_0 K_1 - f_c K_1 - \gamma K_1(1 - p_v)\tau_{\text{ref}} - f_i K_1 \\ &\approx (\gamma K_0 - \gamma \tau_{\text{ref}} - f_c - f_i) K_1 = (\gamma K_0 - \gamma \tau_{\text{ref}} - f_c - f_i) \\ &\quad \cdot \frac{[(x - C_1)(\omega_t + \omega_r) \cos \beta_0 + (y - C_2)(\omega_r - \omega_t) \sin \beta_0 + C_3]}{c + v_0 \sin(\theta - \beta_0)}, \end{aligned} \quad (29)$$

where $C_1 = v_0 \cos \theta \cdot |\mathbf{R}_r(0)|/c$, $C_2 = v_0 \sin \theta \cdot |\mathbf{R}_r(0)|/c$, and $C_3 = v_0^2 \sin(\theta + \beta_0) \cdot \sin \theta \cos \beta_0/c$ are all constant terms.

From above, two problems arise with the B-ISAR Range-Doppler imaging of high-speed targets based on dechirping processing: (a) the calibration factors in the range and cross-range directions are determined by the joint parameters of system and target motion, which are difficult to obtain, and (b) coupling between the range and cross-range occurs in

the Doppler frequency domain, which leads to the geometry distortion of the image.

4. B-ISAR Imaging Method of High-Speed Target Based on Sparse Imaging

Drawing from equations (28) and (29), the range calibration is related to β_0 , θ , and ν_0 , whereas cross-range calibration is related to β_0 , θ , ν_0 , ω_t , and ω_r . Therefore, to obtain a B-ISAR image of a high-speed target with geometric distortion correction and 2D calibration, the five parameters should be estimated first.

Discretizing fast time and slow time into $n(n = 1, \dots, N)$ and $m(m = 1, \dots, M)$, respectively, the imaging area is divided into well-distributed networks of $K \times L$ size according to the intervals of dx and dy . After translation compensation and high-order phase term compensation, the target echo of B-ISAR, as in equation (25), can be discretized into [12]

$$\mathbf{S} = \sum_{k=1}^K \sum_{l=1}^L \mathbf{A}^{k,l} \boldsymbol{\Sigma}_{k,l} + \mathbf{E}, \quad (30)$$

where $\mathbf{A}^{k,l} = [a_{n,m}^{k,l}]_{N \times M}$ is the observation matrix corresponding to the scattering point (k, l) , $\boldsymbol{\Sigma}_{k,l}$ is the scattering coefficient, and \mathbf{E} is the noise matrix. Vectoring equation (30), such as $\mathbf{s} = \text{vec}(\mathbf{S})$, $\boldsymbol{\sigma} = \text{vec}(\boldsymbol{\Sigma})$, $\mathbf{A} = [\text{vec}(\mathbf{A}^{1,1}), \dots, \text{vec}(\mathbf{A}^{K,1}), \text{vec}(\mathbf{A}^{1,2}), \dots, \text{vec}(\mathbf{A}^{K,L})]$, and $\mathbf{e} = \text{vec}(\mathbf{E})$, we obtain

$$\mathbf{s}_{MN \times 1} = \mathbf{A}_{MN \times KL} \boldsymbol{\sigma}_{KL \times 1} + \mathbf{e}_{MN \times 1}, \quad (31)$$

where \mathbf{e} is the noise whose expectation is zero and whose covariance matrix is $\eta \mathbf{I}$, where η is the noise power.

Equation (31) is an underdetermined equation with innumerable solutions. Usually, we limit the range of the solution by the sparsity of $\boldsymbol{\sigma}$, then the solution of equation (31) can be transformed into

$$\begin{aligned} \min \quad & \|\boldsymbol{\sigma}\|_0, \\ \text{s.t.} \quad & \|\mathbf{s} - \mathbf{A}\boldsymbol{\sigma}\|_2^2 \leq \varepsilon. \end{aligned} \quad (32)$$

However, this problem is a NP hard problem, so we should use the L1-norm to approximate the L0-norm, then equation (32) can be transformed into

$$\begin{aligned} \min \quad & \|\boldsymbol{\sigma}\|_1, \\ \text{s.t.} \quad & \|\mathbf{s} - \mathbf{A}\boldsymbol{\sigma}\|_2^2 \leq \varepsilon. \end{aligned} \quad (33)$$

There are many algorithm to solve equation (33), such as greedy algorithm [23], convex optimization algorithm [24], and Bayesian statistical method [25]. However, for robust reconstruction performance and better noise immunity, the Bayesian inference theory is adopted with the maximum a posterior (MAP) criterion. As we know from above, \mathbf{A} is related to the unknown parameters β_0 , θ , ν_0 , ω_t , and ω_r . As $\boldsymbol{\sigma}$ is a parameter to be estimated, the solution of equation

(33) can be transformed into a multiparameter estimation problem. According to the MAP criterion, $\boldsymbol{\sigma}$, η , β_0 , θ , ν_0 , ω_t , and ω_r can be obtained by joint optimization as

$$\begin{aligned} \boldsymbol{\sigma} &= \arg \max_{\boldsymbol{\sigma}} f(\boldsymbol{\sigma}|\mathbf{s}) = \arg \max_{\boldsymbol{\sigma}} \left(\frac{f(\mathbf{s}|\boldsymbol{\sigma})f(\boldsymbol{\sigma})}{f(\mathbf{s})} \right) \\ &= \arg \max_{\boldsymbol{\sigma}} (f(\mathbf{s}|\boldsymbol{\sigma})f(\boldsymbol{\sigma})) \propto \arg \max_{\boldsymbol{\sigma}, \eta, \omega_t, \omega_r, \beta_0, \theta, \nu_0} \\ &\quad \cdot f(\mathbf{s}|\boldsymbol{\sigma}, \eta, \omega_t, \omega_r, \beta_0, \theta, \nu_0) f(\boldsymbol{\sigma}) f(\eta) \\ &\quad \cdot f(\omega_t) f(\omega_r) f(\beta_0) f(\theta) f(\nu_0). \end{aligned} \quad (34)$$

Since $\mathbf{e} \sim CN(0, \eta \mathbf{I})$, the conditional probability density function of the echo \mathbf{s} can be written by

$$f(\mathbf{s}|\boldsymbol{\sigma}, \eta, \omega_t, \omega_r, \beta_0, \theta, \nu_0) = CN(\mathbf{A}\boldsymbol{\sigma}, \eta \mathbf{I}). \quad (35)$$

Assuming that $\boldsymbol{\sigma}$ obeys the Laplacian prior distribution [26], the probability distribution function (PDF) of $\boldsymbol{\sigma}$ is

$$f(\boldsymbol{\sigma}) = \exp(-\lambda \|\boldsymbol{\sigma}\|_1). \quad (36)$$

If the parameters η , β_0 , θ , ν_0 , ω_t , and ω_r all obey the noninformation prior distribution, then

$$f(\eta) f(\omega_t) f(\omega_r) f(\beta_0) f(\theta) f(\nu_0) \propto 1. \quad (37)$$

Substituting equations (35), (36), and (37) into equation (34) and taking the negative logarithm, we can draw the equation as [12]

$$\begin{cases} J(\boldsymbol{\sigma}) = \|\mathbf{s} - \mathbf{A}(\omega_t, \omega_r, \beta_0, \theta, \nu_0)\boldsymbol{\sigma}\|_2^2 + 2\eta \|\boldsymbol{\sigma}\|_1, \\ \left(\widehat{\boldsymbol{\sigma}}, \widehat{\eta}, \widehat{\omega}_t, \widehat{\omega}_r, \widehat{\beta}_0, \widehat{\theta}, \widehat{\nu}_0 \right) = \arg \min_{\boldsymbol{\sigma}, \eta, \omega_t, \omega_r, \beta_0, \theta, \nu_0} \{J(\boldsymbol{\sigma})\}. \end{cases} \quad (38)$$

To overcome the nondifferentiability of L1-norm, a smooth approximation function is introduced as [25]

$$\|\boldsymbol{\sigma}\|_1 = \sum_{kl=1}^{KL} |\sigma_{kl}| \approx \sum_{kl=1}^{KL} (|\sigma_{kl}|^2 + \varsigma)^{1/2}, \quad (39)$$

where ς is a small positive number. Then equation (38) is transformed into

$$\begin{cases} J(\boldsymbol{\sigma}) = \|\mathbf{s} - \mathbf{A}(\omega_t, \omega_r, \beta_0, \theta, \nu_0)\boldsymbol{\sigma}\|_2^2 + 2\eta \sum_{kl=1}^{KL} (|\sigma_{kl}|^2 + \varsigma)^{1/2}, \\ \left(\widehat{\boldsymbol{\sigma}}, \widehat{\eta}, \widehat{\omega}_t, \widehat{\omega}_r, \widehat{\beta}_0, \widehat{\theta}, \widehat{\nu}_0 \right) = \arg \min_{\boldsymbol{\sigma}, \eta, \omega_t, \omega_r, \beta_0, \theta, \nu_0} \{J(\boldsymbol{\sigma})\}. \end{cases} \quad (40)$$

Input: Echo vector \mathbf{s}

Initialization: $\hat{\sigma}^0, \hat{\eta}^0, \hat{\omega}_t^0, \hat{\omega}_r^0, \hat{\beta}_0^0, \hat{\theta}^0, \hat{\nu}_0^0$

Cycle:

(1) **Sparse Imaging**
Fix the parameters $\hat{\omega}_t^i, \hat{\omega}_r^i, \hat{\beta}_0^i, \hat{\theta}^i, \hat{\nu}_0^i$, calculate the observation matrix $\mathbf{A}^i(\hat{\omega}_t^i, \hat{\omega}_r^i, \hat{\beta}_0^i, \hat{\theta}^i, \hat{\nu}_0^i)$, and then solve Equation (42) using the conjugate gradient method.

(2) **Parameter Estimation**
Fix the result $\hat{\sigma}^{i+1}$ of sparse imaging, solve the equation $(\hat{\omega}_t^{i+1}, \hat{\omega}_r^{i+1}, \hat{\beta}_0^{i+1}, \hat{\theta}^{i+1}, \hat{\nu}_0^{i+1}) = \arg \max_{\omega_t, \omega_r, \beta_0, \theta, \nu_0} \|\mathbf{s} - \mathbf{A}(\omega_t, \omega_r, \beta_0, \theta, \nu_0) \hat{\sigma}^{i+1}\|_2^2$ using the linear search method [12], golden section search method [29], or some intelligent algorithms, such as particle swarm optimization [30].

(3) **Iteration Judgment**
When $\hat{\sigma}$ satisfies the convergence condition $\|\hat{\sigma}^{i+1} - \hat{\sigma}^i\|_2 / \|\hat{\sigma}^{i+1}\|_2 < \zeta_\sigma$, the cycle stops, otherwise, the cycle will continue until the algorithm converges.

Output: the imaging result $\hat{\sigma}$ and estimated parameters $\hat{\eta}, \hat{\omega}_t, \hat{\omega}_r, \hat{\beta}_0, \hat{\theta}, \hat{\nu}_0$.

ALGORITHM 1: Flow chart of the sparse imaging algorithm.

Obtain the conjugate gradient of σ from the cost function $J(\sigma)$:

$$\nabla J_{\sigma^*}(\sigma) = \mathbf{H}(\sigma)\sigma - 2\mathbf{A}^H\mathbf{s}, \quad (41)$$

where $\mathbf{H}(\sigma) = 2\mathbf{A}^H\mathbf{A} + 2\eta\Lambda(\sigma)$, which can be regarded as the Hessian matrix of the cost function [25], $\Lambda(\sigma) = \text{diag}[1/\sqrt{|\sigma_{kl}|^2 + \zeta}]$, ($kl = 1, 2, \dots, KL$). According to the Newton method [27], we can obtain the iterative solution as

$$\begin{aligned} \sigma^{w+1} &= \sigma^w - [\mathbf{H}(\sigma^w)]^{-1} \nabla J_{\sigma^*}(\sigma^w) \\ &= \sigma^w - [\mathbf{H}(\sigma^w)]^{-1} [\mathbf{H}(\sigma^w)\sigma^w - 2\mathbf{A}^H\mathbf{s}] \\ &= [\mathbf{A}^H\mathbf{A} + \eta\Lambda(\sigma^w)]^{-1} \mathbf{A}^H\mathbf{s}. \end{aligned} \quad (42)$$

Calculate the inverse matrix directly has a higher complexity, so we can use the conjugate gradient method [28] to solve equation (42).

However, \mathbf{A} is related to the unknown parameters $\beta_0, \theta, \nu_0, \omega_t$, and ω_r , which should be estimated before solving equation (42). So we use the expectation maximization (EM) algorithm to decompose equation (40) into two processes and solve them alternately and iteratively: (a) the sparse imaging process, by fixing the parameters $\beta_0, \theta, \nu_0, \omega_t$, and ω_r to optimize σ and η ; and (b) the parameter estimation process, by fixing σ and η to estimate the parameters $\beta_0, \theta, \nu_0, \omega_t$, and ω_r . The details of the process are shown in Algorithm 1.

5. Simulation Experiment

The target is composed of 33 scattering points, and its model is shown in Figure 2. Assuming that the target motion is stable, the velocity is 2000 m/s, whose angle with the x -axis is 60° . At $t_m = 0$, the half bistatic angle is $\beta_0 = 20^\circ$, and the distances from the target to the transmitter and receiver are

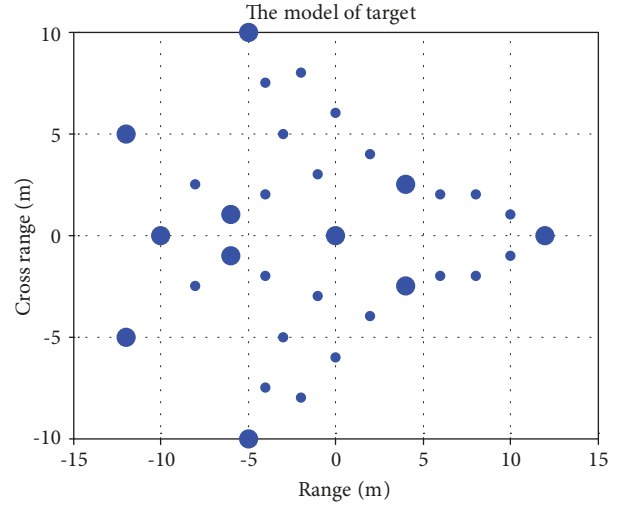


FIGURE 2: The scattering model of the high-speed target.

$R_t(0) = 60$ km and $R_r(0) = 30$ km, respectively. The transmitted signal is LFM, the bandwidth is 600 MHz, the carrier frequency is 10 GHz, the pulse width is 200 μ s, the pulse repetition frequency is 100 Hz, the pulse number is 100, and the sampling frequency is 10 MHz.

5.1. *Pulse Compression Based on the Speed Compensation.* From equation (28), using the 3 dB width of the Sinc function to represent the resolution, the range resolution is

$$\rho_r = \Delta f_i T_p \cdot \frac{c + \nu_0 \sin(\theta - \beta_0)}{2B \cos \beta_0} \approx \frac{\Delta f_i T_p c}{2B \cos \beta_0}. \quad (43)$$

Substituting the system parameters into this equation, we obtain $\rho_r \approx 0.177$ m. If the target migration distance in a pulse is less than ρ_r ($\Delta_r = \nu t_p \sin(\theta) = 0.035$ m), it can be neglected, as the speed has no effect on the pulse compression, as shown in Figure 3(a). However, when the speed does not satisfy $\nu \ll c$, the speed can be calculated from the set parameters where the migration distance is $\Delta_r =$

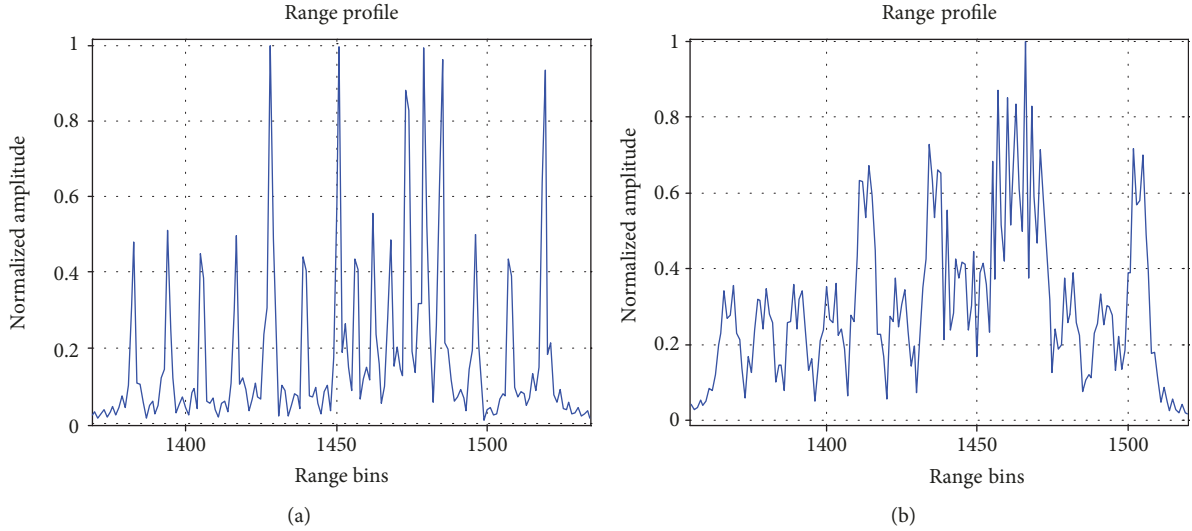


FIGURE 3: The output of the narrowband matched filter: (a) the output after pulse compression when $v=200$ m/s; (b) the output after pulse compression when $v=2000$ m/s.

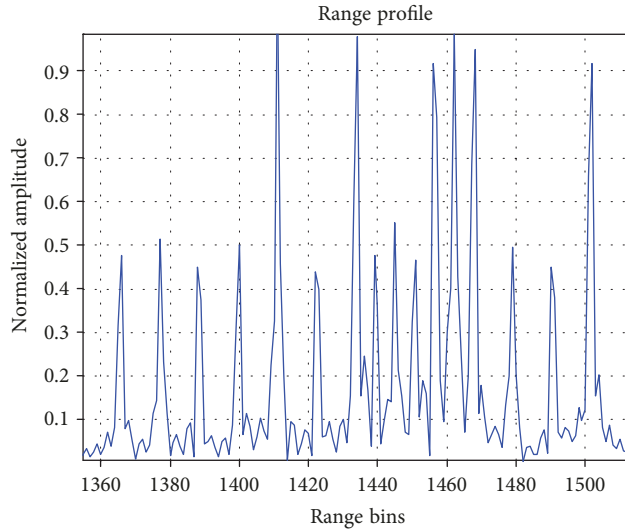


FIGURE 4: The output after speed compensation.

$vt_p \sin(\theta) = 0.346$ m at this time, which cannot be neglected. From Section 2.2, the high-speed motion leads to the intra-pulse modulation of the echo, which results in the peak splitting of the range profile, as shown in Figure 3(b).

From Figure 3, the high-speed motion of the target causes the spread and splitting of the peak of the range profile, so the range of the scattering points cannot be correctly indicated. Thus, 2D image may be blurred and defocused. To address this problem, as described in Section 3.1, the discrete chirp transform is used for estimating the chirp rate, with which the speed compensation function can be constructed. The output after pulse compression is shown in Figure 4.

5.2. Doppler Compensation Based on Parameter Estimation by Using the CPF. From equation (24), after the speed and translational compensation, the echo can be regarded as a cubic phase function with respect to t_m in the cross-range direction. The high-order phase term will lead to a defocused

image, as shown in Figures 5(a) and 5(c). Similarly, as described in Section 3.2, the coefficients of the high-order phase term can be estimated by using the CPF method. With them, the Doppler compensation function can be constructed. After Doppler compensation, the cross range profile and the 2D image are shown in Figures 5(b) and 5(d).

The image entropy is usually used to measure the image quality. Assuming that the amplitude of each pixel in image $\mathbf{I}_{P \times Q}$ is $I(p, q)$, the total amplitude of the image is $S = \sum_p \sum_q |I(p, q)|$, and then the entropy of the image is

$$\begin{aligned}
 H &= \sum_{p=1}^P \sum_{q=1}^Q \frac{|I(p, q)|}{S} \ln \frac{S}{|I(p, q)|} \\
 &= \ln S - \frac{1}{S} \sum_{p=1}^P \sum_{q=1}^Q |I(p, q)| \ln |I(p, q)|.
 \end{aligned} \tag{44}$$

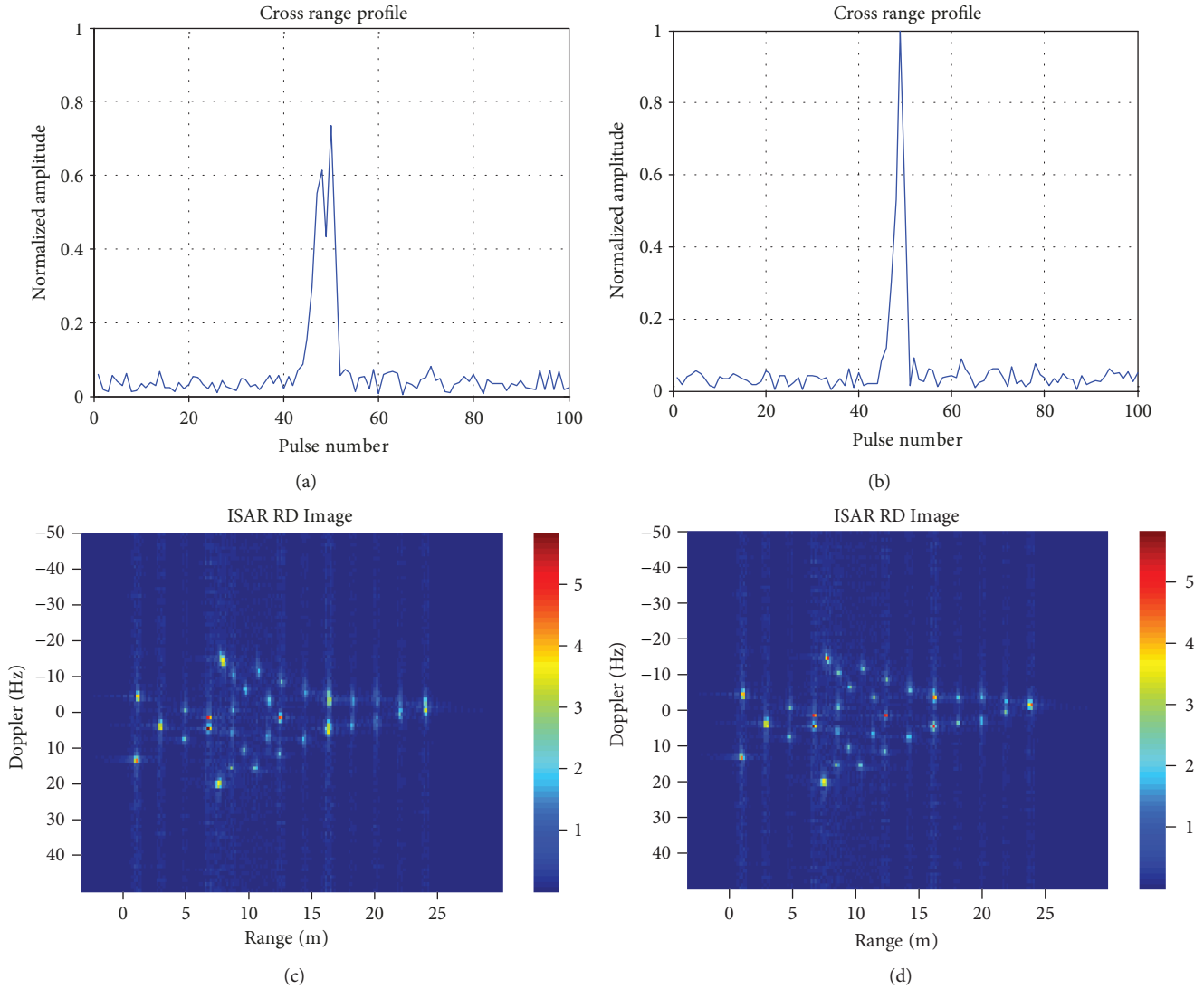


FIGURE 5: Imaging results of the cross-range profile (a) before and (b) after Doppler compensation, and imaging results of the Range-Doppler algorithm (RDA) imaging result (c) before and (d) after Doppler compensation.

TABLE 1: Image entropy.

Figure	Image entropy
5c	4.3941
5d	4.3816

The image entropy of each image in Figures 5(c) and 5(d) according to equation (44) is shown in Table 1.

From the comparison of Figures 5(a)–5(d) and Table 1, after Doppler compensation, the image of the target is more focused in a cross-range direction and the image entropy of the image is smaller.

5.3. B-ISAR Imaging of High-Speed Target Based on the Sparse Imaging. Assume that the size of the uniform 2D grid is 50×30 , with the intervals of $dx = 0.5$ m and $dy = 1$ m. The EM algorithm is used to image the target according to the flow chart shown in Algorithm 1 and is compared with the

RDA result, as shown in Figure 6. Among them, Figure 6(a) shows the RDA result without speed or Doppler compensation. As a result, the image is defocused in both the range and cross-range directions. Figure 6(b) is the RDA result with Doppler compensation but without speed compensation, and the image is defocused in the range direction. In contrast, Figure 6(c) shows the RDA result with speed compensation but without Doppler compensation, so the image is defocused in the cross-range direction. Figure 6(d) shows the RDA result with joint speed and Doppler compensation, and the image is focused. However, it is not calibrated and there is geometric distortion. Figure 6(e) shows the result using the sparse imaging previously proposed [12]. The side-lobe is so high that we cannot achieve a clear image with calibration and distortion correction. Figure 6(f) shows the result of the proposed sparse imaging method with joint speed and Doppler compensation. Both the range and cross range of the image are focused, and the geometric distortion correction and calibration are both realized.

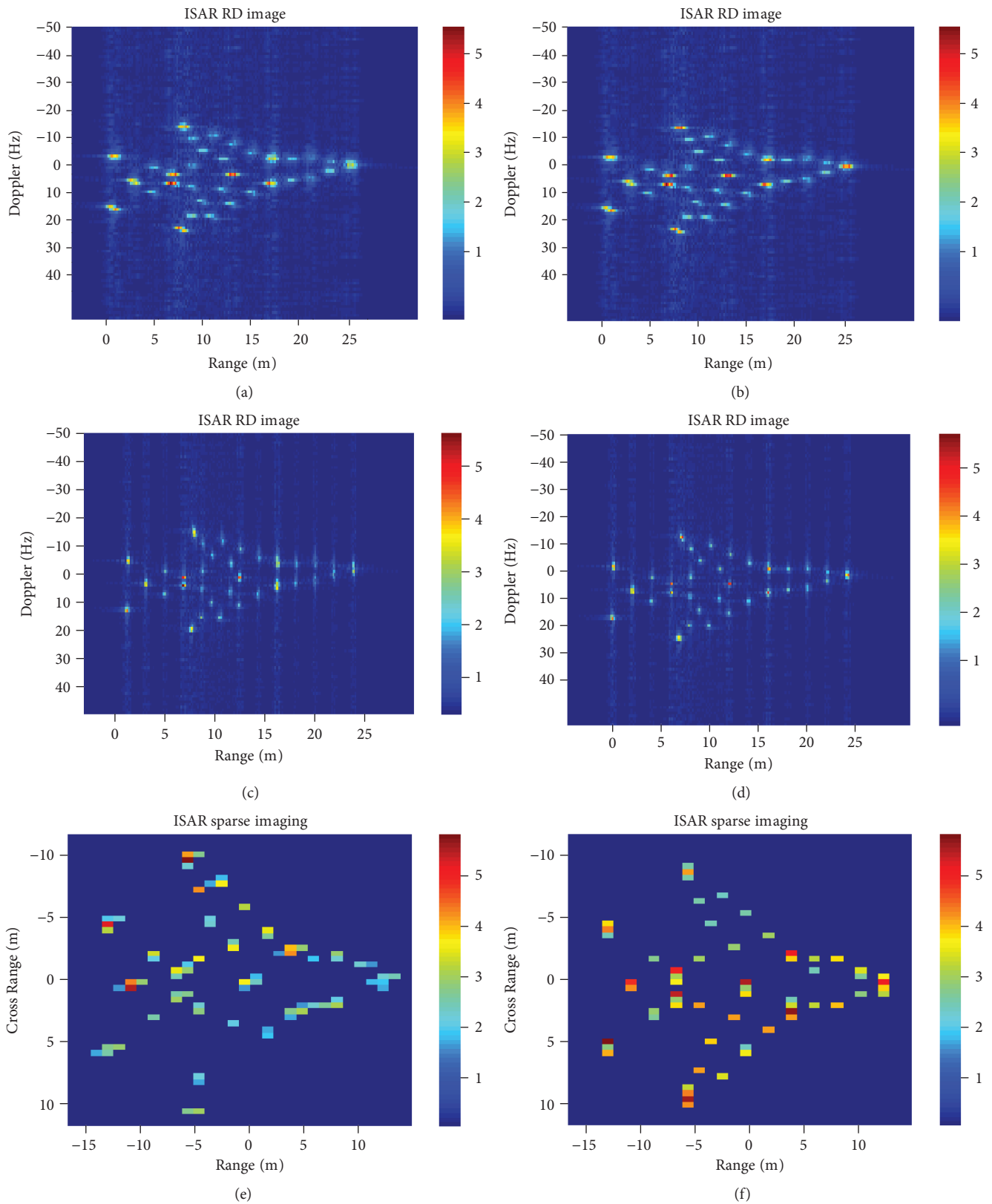


FIGURE 6: The imaging result: (a) RDA result without speed or Doppler compensation; (b) RDA result without speed compensation; (c) RDA result without Doppler compensation; (d) RDA result with joint speed and Doppler compensation; (e) sparse imaging result without speed or Doppler compensation; and (f) sparse imaging result with joint speed and Doppler compensation.

TABLE 2: Image entropy.

Figure	Image entropy
6a	4.4023
6b	4.3951
6c	4.3941
6d	4.3816
6e	3.1644
6f	3.1474

The image entropy of each image in Figures 6(a)–6(f) is shown in Table 2.

From the comparison in Figures 6(a)–6(c) and Table 2, the high-speed motion causes the peak splitting of the range profile and the spectrum spread in a cross-range direction, blurring and defocusing the image. If the model mentioned by Chai et al. [12] to achieve sparse imaging is adopted, the sidelobe is high and the distortion correction is incomplete, so the image quality is poor, as shown in Figure 6(e). Using speed and Doppler compensation to eliminate the high-order phase terms generated by the high-speed motion of the target, a clearer image can be obtained, as in Figure 6(d). However, two challenges remain: directly estimating the calibration factor and fixing the geometric distortion in the image. To solve these issues, the proposed method uses the sparsity of the scattering points to simultaneously perform sparse imaging with geometric distortion correction and calibration. The result is shown in Figure 6(f). From the comparison of Figures 6(a), 6(e), and 6(f) and Table 2, the proposed method can not only complete the sparse imaging of high-speed moving targets with high quality but also attain the distortion correction and calibration.

5.4. Verification of the Parameter Estimation Accuracy. The difference between the method proposed in Section 4 and the method proposed in [12] is the introduction of speed compensation and Doppler compensation, and the cost time of these two parts can be calculated according to [20–22]. However, the computation complexity of the sparse imaging step is the same as the method in [12].

Otherwise, the key point of the sparse imaging algorithm is transforming the joint imaging, geometric distortion correction, and calibration problem into a parameter estimation problem. Therefore, the accuracy of parameter estimation plays an important role in the imaging quality. Known from Section 4, the sparse imaging method with geometric distortion correction and calibration can be transformed into an estimation problem of parameters β_0 , θ , ν_0 , ω_t , and ω_r . Due to the time-varying property of B-ISAR imaging geometry, the real values of ω_t and ω_r are hard to obtain. So, we mainly validated the accuracy of the parameters β_0 , θ , and ν_0 . The results of Monte Carlo simulation under different signal-to-noise ratio (SNR) conditions are shown in Figures 7–9. And the SNR defined in this paper is the SNR minus the gain of pulse compression ($D = 10 \log_{10}(B \cdot t_p) = 50.79$ dB).

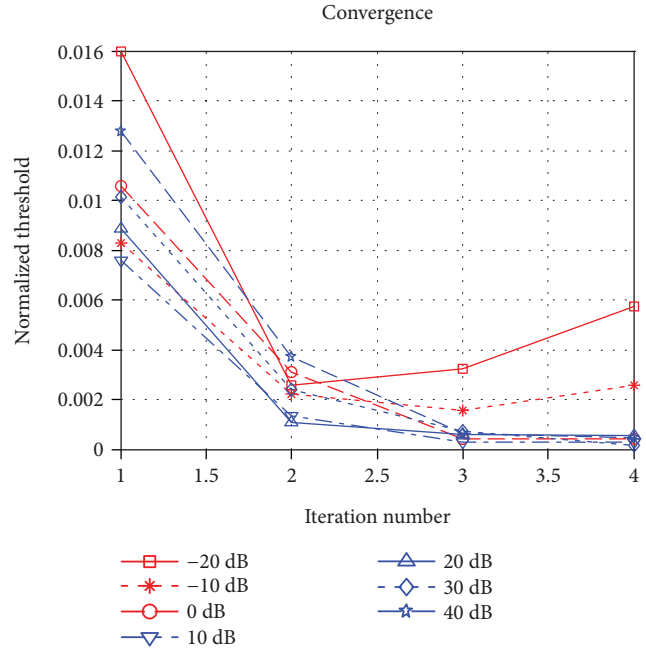


FIGURE 7: Convergence curve of the normalized threshold.

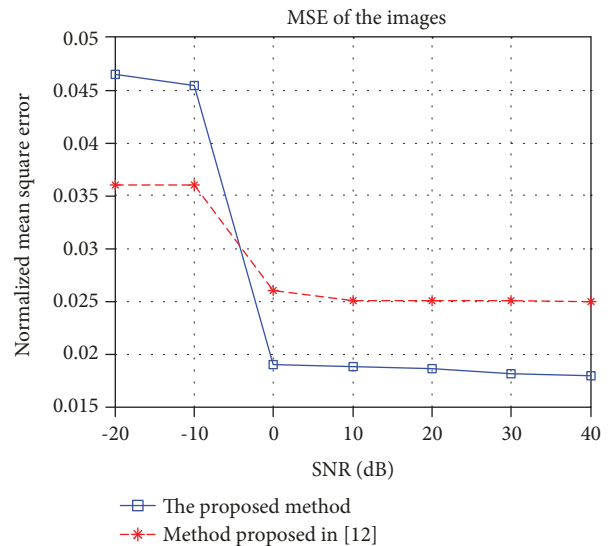
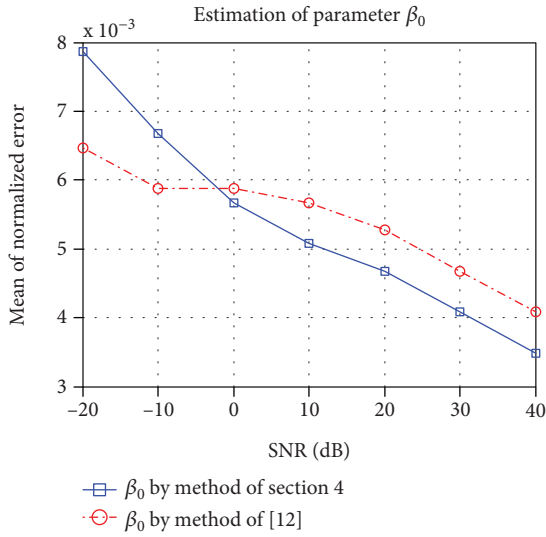


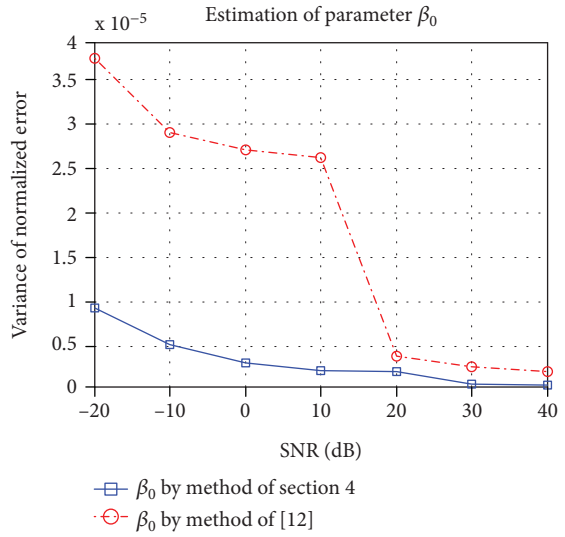
FIGURE 8: Mean square error of the image.

At first, Figure 7 shows the convergence of the proposed method. Due to the conjugate gradient method, the convergence speed of the proposed algorithm is fast and is almost independent of the SNR when $\text{SNR} \geq 0$ dB.

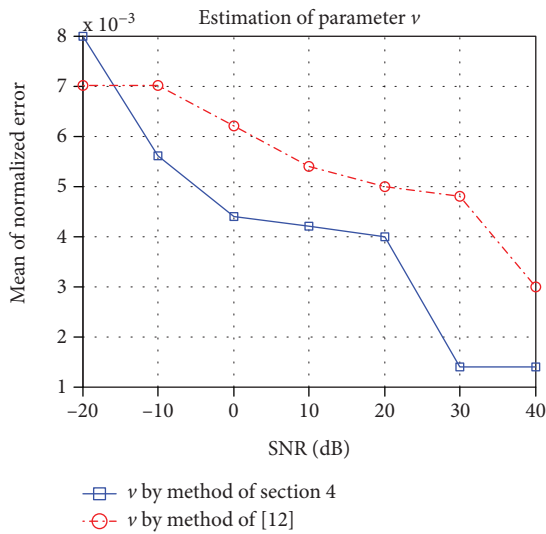
Then, the normalized mean square errors (NMSE) between the sparse imaging results and the target's scattering model are shown in Figure 8. Compared to the method proposed in [12], when SNR is lower than 10 dB, the image NMSE of the proposed method is higher, because the DCFT method and CPF method is sensitive to the noise. When SNR increases to above 0 dB, the image NMSE of the proposed method is lower, meaning the imaging quality of the proposed method is better.



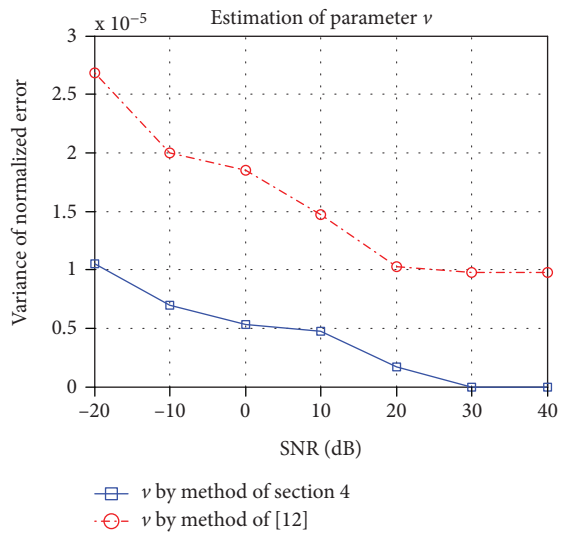
(a)



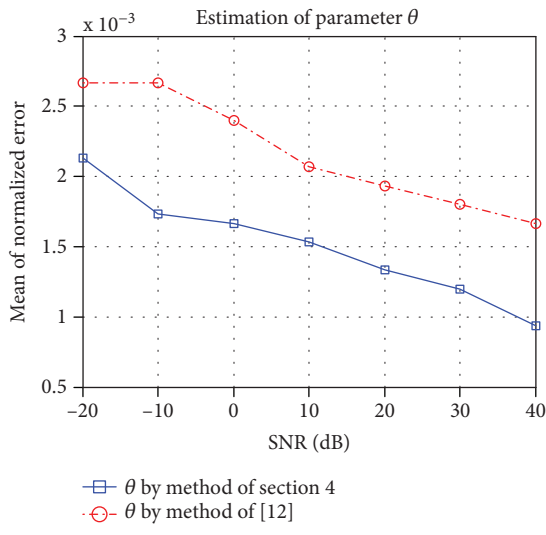
(b)



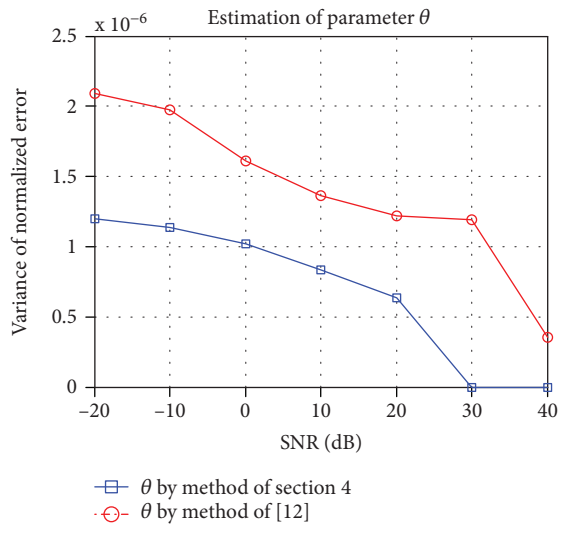
(c)



(d)



(e)



(f)

FIGURE 9: Mean value of the normalized error of (a) β_0 , (c) ν , and (e) θ ; and variance of the normalized error of (b) β_0 , (d) ν , and (f) θ .

At last, Figure 9 shows the parameter estimation accuracy. Figures 9(a), 9(c), and 9(e) is the mean values of normalized estimation error of β_0 , v , and θ versus SNR compared to the method proposed in [12], respectively, and Figures 9(b), 9(d), and 9(f) is their variances.

From Figures 9(a) and 9(f), when SNR is greater than 0 dB, the estimated values of the proposed method are closer to the true values of β_0 , v , and θ , which indicates that the proposed algorithm can estimate parameters with higher accuracy than the method proposed in [12].

6. Conclusion

For the practical problems affecting the B-ISAR imaging of high-speed moving targets, the original methods based on the monostatic ISAR equivalent idea and the motion decomposition method both rely on the “stop-go” model, which assumes that no migration occurs in an echo pulse. However, the high-speed motion does not satisfy this assumption, which causes the intrapulse modulation of the echoes, resulting in the peak splitting of the range profile and the spread of the Doppler spectrum, ultimately affecting the imaging quality. In this paper, the B-ISAR echo model of a high-speed target is established based on motion decomposition. The speed

and Doppler compensation are used to eliminate the high-order phase term that leads to the defocused image. After compensation, the analytical formula of the geometric distortion and calibration factors can be deduced, and a sparse imaging algorithm, with geometric distortion correction and calibration, was proposed by using the sparsity of the scattering points. Simulation results show that the proposed method can effectively achieve geometric distortion correction and calibration of an image while completing sparse imaging, and the image has good resolution.

Appendix

A. Proof of Equation (20)

Known from the B-ISAR imaging geometry shown in Figure 1, the radial velocities of target relative to the transmitter and receiver are

$$v_{Tm} = v_0 \cos [90^\circ - \theta - \beta_t(t_m)] = v_0 \sin [\theta + \beta_t(t_m)], \quad (\text{A.1})$$

$$v_{Rm} = v_0 \cos [90^\circ - \theta + \beta_r(t_m)] = v_0 \sin [\theta - \beta_r(t_m)]. \quad (\text{A.2})$$

Substituting equations (A.1) and (A.2) into equation (19),

$$\begin{aligned} \tau_{im} &= \frac{[c + v_0 \sin(\theta - \beta_r(t_m))] \cdot [|\mathbf{R}_t(t_m)| + x \sin \beta_t(t_m) + y \cos \beta_t(t_m)]}{c(c + v_{Rm})} \\ &+ \frac{[c - v_0 \sin(\theta + \beta_t(t_m))] \cdot [|\mathbf{R}_r(t_m)| - x \sin \beta_r(t_m) + y \cos \beta_r(t_m)]}{c(c + v_{Rm})} \\ &= \frac{|\mathbf{R}_t(t_m)| + |\mathbf{R}_r(t_m)|}{c} + \frac{v_0(x \sin \theta - y \cos \theta) \cdot \sin[\beta_t(t_m) + \beta_r(t_m)]}{c(c + v_{Rm})} \\ &+ \frac{(x - (v_0 \cos \theta \cdot |\mathbf{R}_r(t_m)|/c)) \cdot [\sin \beta_t(t_m) - \sin \beta_r(t_m)]}{c + v_{Rm}} \\ &+ \frac{(y - (v_0 \sin \theta \cdot |\mathbf{R}_r(t_m)|/c)) [\cos \beta_t(t_m) + \cos \beta_r(t_m)]}{c + v_{Rm}}. \end{aligned} \quad (\text{A.3})$$

Assuming that the target motion is stable during the imaging period, the rotation angles of the target relative to the transmitter and receiver are small enough, then $\sin(\omega_t t_m) \approx \omega_t t_m$, $\cos(\omega_t t_m) \approx 1$, $\sin(\omega_r t_m) \approx \omega_r t_m$, and $\cos(\omega_r t_m) \approx 1$. Substituting these into $\beta_t(t_m)$ and $\beta_r(t_m)$, then we obtain

$$\begin{cases} \sin[\beta_t(t_m)] \approx \sin \beta_0 + \omega_t t_m \cdot \cos \beta_0, \\ \sin[\beta_r(t_m)] \approx \sin \beta_0 - \omega_r t_m \cdot \cos \beta_0, \\ \cos[\beta_t(t_m)] \approx \cos \beta_0 - \omega_t t_m \cdot \sin \beta_0, \\ \cos[\beta_r(t_m)] \approx \cos \beta_0 + \omega_r t_m \cdot \sin \beta_0. \end{cases} \quad (\text{A.4})$$

There is usually $x, y \ll |\mathbf{R}_t(t_m)|$, so equation (A.3) can be approximated as

$$\begin{aligned} \tau_{im} &\approx \frac{|\mathbf{R}_t(t_m)| + |\mathbf{R}_r(t_m)|}{c} \\ &+ \frac{2(y - (v_0 \sin \theta \cdot |\mathbf{R}_r(t_m)|/c)) \cdot \cos \beta_0}{c + v_{Rm}} \\ &+ \frac{(x - (v_0 \cos \theta \cdot |\mathbf{R}_r(t_m)|/c)) \cdot (\omega_t + \omega_r) t_m \cdot \cos \beta_0}{c + v_{Rm}} \\ &+ \frac{(y - (v_0 \sin \theta \cdot |\mathbf{R}_r(t_m)|/c)) \cdot (\omega_r - \omega_t) t_m \cdot \sin \beta_0}{c + v_{Rm}}. \end{aligned} \quad (\text{A.5})$$

When v_0 is small enough (satisfies $(v_0|\mathbf{R}_r(t_m)|)/(c^2) \ll 1$) and $\theta = 0$, equation (A.5) can be simplified as

$$\tau_{im} \approx \frac{|\mathbf{R}_t(t_m)| + |\mathbf{R}_r(t_m)|}{c} + \frac{2y \cos \beta_0 + x(\omega_t + \omega_r)t_m \cos \beta_0 + y(\omega_r - \omega_t)t_m \sin \beta_0}{c}, \quad (\text{A.6})$$

which is the same as the formula previously derived [12]. When $(v_0|\mathbf{R}_r(t_m)|)/(c^2) \ll 1$ is not satisfied, with the knowledge of

$$\begin{aligned} |\mathbf{R}_r(t_m)| &= |\mathbf{R}_r(0)| + v_{Rm}t_m \\ &\approx |\mathbf{R}_r(0)| + v_0 \sin(\theta - \beta_0) \cdot t_m \\ &\quad + v_0 \omega_r \cos(\theta - \beta_0) \cdot t_m^2. \end{aligned} \quad (\text{A.7})$$

We can obtain

$$\begin{aligned} \tau_{im} &\approx \frac{|\mathbf{R}_t(t_m)| + |\mathbf{R}_r(t_m)|}{c} + \frac{2y \cos \beta_0 + x(\omega_t + \omega_r)t_m \cos \beta_0 + y(\omega_r - \omega_t)t_m \sin \beta_0}{c + v_{Rm}} \\ &\quad - \frac{(v_0/c) \cdot |\mathbf{R}_r(t_m)| \cdot [2 \sin \theta \cos \beta_0 + \cos \theta \cos \beta_0 (\omega_t + \omega_r)t_m + \sin \theta \sin \beta_0 (\omega_r - \omega_t)t_m]}{c + v_{Rm}} \\ &\approx K_0 + K_1 t_m + K_2 t_m^2 + K_3 t_m^3, \end{aligned} \quad (\text{A.8})$$

where

$$\begin{aligned} K_0 &\approx \frac{|\mathbf{R}_t(0)| + |\mathbf{R}_r(0)|}{c} + \frac{2y \cos \beta_0 - (2v_0/c) \cdot |\mathbf{R}_r(0)| \cdot \sin \theta \cos \beta_0}{c + v_0 \sin(\theta - \beta_0)}, \\ K_1 &\approx \frac{(x - (v_0 \cos \theta \cdot |\mathbf{R}_r(0)|/c))(\omega_t + \omega_r) \cos \beta_0 + (y - (v_0 \sin \theta \cdot |\mathbf{R}_r(0)|/c))(\omega_r - \omega_t) \sin \beta_0 + 2v_0 \sin \theta \cos \beta_0}{c + v_0 \sin(\theta - \beta_0)}, \\ K_2 &\approx \frac{(v_0^2/c) \cdot \sin(\theta - \beta_0) \cdot [\omega_r \cos(\theta - \beta_0) + \omega_t \cos(\theta + \beta_0)]}{c + v_0 \sin(\theta - \beta_0)} + \frac{(v_0^2/c) \cdot \omega_r \cos(\theta - \beta_0) \cdot 2 \sin \theta \cos \beta_0}{c + v_0 \sin(\theta - \beta_0)}, \\ K_3 &\approx \frac{(v_0^2/c) \cdot \omega_r \cos(\theta - \beta_0) \cdot [\omega_r \cos(\theta - \beta_0) + \omega_t \cos(\theta + \beta_0)]}{c + v_0 \sin(\theta - \beta_0)}. \end{aligned} \quad (\text{A.9})$$

Since $v_0^2 \ll c^2$, K_2 and K_3 are usually negligible. So equation (A.8) can be simplified as

$$\tau_{im} \approx K_0 + K_1 t_m. \quad (\text{A.10})$$

Data Availability

No data were used to support this study.

Disclosure

The research did not receive specific funding but was performed as part of the employment of Space Engineering University.

Conflicts of Interest

The authors declare that there is no conflict of interest regarding the publication of this paper.

References

- [1] J. Zheng, H. Liu, Z. Liu, and Q. Liu, "ISAR imaging of ship targets based on an integrated cubic phase bilinear autocorrelation function," *Sensors*, vol. 17, no. 3, p. 498, 2017.
- [2] J. Xu, J. Cai, Y. Sun, X. G. Xia, A. Farina, and T. Long, "Efficient ISAR phase autofocus based on eigenvalue decomposition," *IEEE Geoscience and Remote Sensing Letters*, vol. 14, no. 12, pp. 2195–2199, 2017.
- [3] M. Martorella, D. Cataldo, and S. Briskin, "Bistatically equivalent monostatic approximation for bistatic ISAR," in *Proceedings of the 2013 IEEE Radar Conference*, pp. 1–5, Ottawa, ON, Canada, 2013.
- [4] V. C. Chen, A. Des Rosiers, and R. Lipps, "Bi-static ISAR Range-Doppler imaging and resolution analysis," in *Proceedings of the 2009 IEEE Radar Conference*, pp. 1–5, Pasadena, CA, USA, 2009.
- [5] W. L. Feng, W. Wei, and F. F. Liu, "Modified Keystone processing algorithm for the space-based bistatic radar systems," in *Proceedings of the 2015 IET Radar Conference*, pp. 1–6, Hangzhou, China, 2016.

- [6] M. Martorella, J. Palmer, J. Homer, B. Littleton, and I. D. Longstaff, "On bistatic inverse synthetic aperture radar," *IEEE Transactions on Aerospace and Electronic Systems*, vol. 43, no. 3, pp. 1125–1134, 2007.
- [7] B. F. Guo, J. L. Wang, and M. G. Gao, "Research on spatial-variant property of bistatic ISAR imaging plane of space target," *Chinese Physics B*, vol. 24, no. 4, pp. 48402–48520, 2015.
- [8] S. Sibó, Y. Yeshu, and J. Yicheng, "Bistatic inverse synthetic aperture radar imaging method for maneuvering targets," *Journal of Applied Remote Sensing*, vol. 10, no. 4, p. 45016, 2016.
- [9] M. S. Kang, B. S. Kang, S. H. Lee, and K. T. Kim, "Bistatic-ISAR distortion correction and range and cross-range scaling," *IEEE Sensors Journal*, vol. 17, no. 16, pp. 5068–5078, 2017.
- [10] B. S. Kang, J. H. Bae, M. S. Kang, E. Yang, and K. T. Kim, "Bistatic-ISAR cross-range scaling," *IEEE Transactions on Aerospace and Electronic Systems*, vol. 53, no. 4, pp. 1962–1973, 2017.
- [11] D. Cataldo and M. Martorella, "Super-resolution for bistatic distortion mitigation," in *Proceedings of the 2016 IEEE Radar Conference*, pp. 1–6, Philadelphia, PA, USA, 2016.
- [12] S. Chai, W. Chen, and C. Chen, "Sparse fusion imaging for a moving target in T/R-R configuration," *Sensors*, vol. 14, no. 6, pp. 10664–10679, 2014.
- [13] S. Zhang, S. Sun, W. Zhang, Z. Zong, and T. Soon Yeo, "High-resolution bistatic ISAR image formation for high-speed and complex-motion targets," *IEEE Journal of Selected Topics in Applied Earth Observations and Remote Sensing*, vol. 8, no. 7, pp. 3520–3531, 2015.
- [14] B. Xiao, S. S. Zhang, and H. Lu, "Bistatic ISAR analysis of high speed space target with linear frequency modulated signal," in *Proceedings of the 2012 European Conference on Synthetic Aperture Radar*, pp. 23–26, Nuremberg, Germany, 2012.
- [15] N. Han, C. X. Shang, and J. Dong, "Bistatic ISAR speed compensation method for space target in one-dimension range profile," *Journal of Astronautics*, vol. 33, no. 4, pp. 505–513, 2012.
- [16] B. F. Guo and C. X. Shang, "Research on bistatic ISAR coherent imaging of space high speed moving target," in *Proceedings of the 2014 IEEE Workshop on Electronics, Computer and Applications*, pp. 205–209, Ottawa, Canada, 2014.
- [17] D. J. Feng, X. S. Wang, S. P. Xiao, and G. Y. Wang, "Phase signatures and compensating approach to moving target echoes by dechirping processing," *Journal of Electronics and Information Technology*, vol. 30, no. 4, pp. 916–920, 2008.
- [18] W. M. Luo and Y. L. Cui, "Novel algorithm of high-speed target ISAR imaging based on stretch method," *Journal of Astronautics*, vol. 25, no. 5, pp. 541–545, 2004.
- [19] X. Ai, Y. Li, X. Wang, and S. Xiao, "Some results on characteristics of bistatic high-range resolution profiles for target classification," *IET Radar, Sonar and Navigation*, vol. 6, no. 5, pp. 379–388, 2012.
- [20] J. Li, B. Li, Z. Guo, M. Liu, and Y. Guo, "Multicomponent chirp signal detection based on discrete chirp-Fourier transform," *Wireless Personal Communications*, vol. 96, no. 3, pp. 4385–4397, 2017.
- [21] L. Zhang, T. Su, Z. Liu, and X. He, "High resolution ISAR imaging in receiver centered region area in bistatic radar," *EURASIP Journal on Advances in Signal Processing*, vol. 2013, no. 1, 2013.
- [22] I. Djurović, M. Simeunović, and P. Wang, "Cubic phase function: A simple solution to polynomial phase signal analysis," *Signal Processing*, vol. 135, pp. 48–66, 2017.
- [23] A. Khwaja and M. Cetin, "Compressed sensing ISAR reconstruction considering highly maneuvering motion," *Electronics*, vol. 6, no. 1, p. 21, 2017.
- [24] C. Ma, B. P. Ng, and J. Feng, "ISAR imaging based on L1 L0 norms homotopy 2D block sparse signal recovery algorithm," *Progress In Electromagnetics Research C*, vol. 67, pp. 135–141, 2016.
- [25] M. Wu, L. Zhang, X.-G. Xia, and M.-D. Xing, "Phase adjustment for polarimetric ISAR with compressive sensing," *IEEE Transactions on Aerospace and Electronic Systems*, vol. 52, no. 4, pp. 1592–1606, 2016.
- [26] L. Zhang, H. Wang, and Z.-j. Qiao, "Resolution enhancement for ISAR imaging via improved statistical compressive sensing," *EURASIP Journal on Advances in Signal Processing*, vol. 2016, no. 1, 2016.
- [27] H. Zhou, D. Alexander, and K. Lange, "A quasi-Newton acceleration for high-dimensional optimization algorithms," *Statistics and Computing*, vol. 21, no. 2, pp. 261–273, 2011.
- [28] E. K. P. Chong and S. H. Zak, *An Introduction to Optimization*, John Wiley & Sons, Inc. Publication, 4th edition, 2013.
- [29] Y. Liu, J. Zou, S. Y. Xu, and Z. P. Chen, "Nonparametric rotational motion compensation technique for high-resolution ISAR imaging via golden section search," *Progress In Electromagnetics Research M*, vol. 36, pp. 67–76, 2014.
- [30] L. Liu, M. S. Qi, and F. Zhou, "A novel non-uniform rotational motion estimation and compensation method for maneuvering targets ISAR imaging utilizing particle swarm optimization," *IEEE Sensors Journal*, vol. 18, no. 1, pp. 299–309, 2018.



Hindawi

Submit your manuscripts at
www.hindawi.com

